Studies of interfacial wave properties during displacement with pure viscoelastic fluids in microchannels (EP)

Seng Hoe Hue, (iD) Loïc Chagot, (iD) and Panagiota Angeli[a] (iD)

AFFILIATIONS

ThAMeS Multiphase, Department of Chemical Engineering, University College London, Torrington Place, London WC1E 7JE, United Kingdom

Note: This paper is part of the special topic, Microscopic Channel Flows.
[a]Author to whom correspondence should be addressed: p.angeli@ucl.ac.uk

ABSTRACT

In this study, new experimental data for the displacement of a Newtonian liquid by three pure viscoelastic (Boger) fluids with different relaxation times were obtained with imaging in a $500\,\mu m$ microchannel. Results were compared against those from displacement using a Newtonian liquid. Small irregular waves were observed at the interface for the Newtonian displacement, while periodic instabilities were seen for all Boger fluid cases. The elastic Mach number (Ma), describing the ratio of the flow velocity with the elastic wave propagation velocity, was found to be the key parameter for correlating the wave properties in the case of Boger fluids. The amplitude of the wavy interface initially increased up to $Ma = 0.5$, before decreasing again. The frequency and the wave velocity increased monotonically with increasing Ma. For all configurations, a phase shift of π was found between the top and the bottom interfaces. Correlations from experimental data were developed for all wave properties. Based on these correlations, an empirical wave model was developed to describe the observed planar images and to reconstruct the three-dimensional waves, which resemble a helical structure.

INTRODUCTION

Fluid displacement is a process used in many chemical and physical applications, for example, in cleaning, food production, and oil extraction. In this process, a functional fluid (displacing phase) is used to remove another fluid (displaced phase). One of the more prominent examples of fluid displacement is the extraction of crude oil from porous rocks in enhanced oil recovery (EOR). Many studies have considered displacement in porous materials, from simple gas injections to more complex chemical flooding techniques, which use additives such as surfactants, polymers, and ionic liquids.[1–3] Reducing the interfacial tension force with surfactants and increasing the viscosity of the displacing phase with polymers have shown to increase the amount of fluid removed and the overall effectiveness of the process. Even though the use of polymeric fluids improves displacement, it introduces complex non-Newtonian phenomena, which have not been studied thoroughly.

Earlier studies of fluid displacement considered only Newtonian fluids in different channel configurations, including Hele–Shaw cells,[4–6] porous media,[7–12] channels with different cross sections such as square[13–15] and triangular,[16] as well as rough[17,18] and open channels.[18,19] In all cases, if the displaced phase has a higher density or viscosity compared to the displacing phase, the flows are unstable, and viscous fingering appears. Viscous fingering leaves a film of the displaced phase on the channel wall[13,20–26] and greatly reduces the displacement efficiency of the system.[27–31]

Following the initial viscous finger, the interface between the two phases destabilizes, and interfacial waves are formed. At this point, the displacement flow resembles an annular flow, with the core fluid representing the displacing phase and the fluid in the annulus representing the displaced phase. The source of the instability is the velocity gradient difference between the two sides of the interface due to the differences in viscosity and density of the two phases.[32,33] There is instability even if the two phases are miscible but with different densities and viscosities.[30,34–45] In addition, different instability patterns have been observed, such as sausage and bamboo core, wavy interface, plug flow, and dispersed flow.[46–52] In the series of papers by Joseph and

co-workers,[53–57] the stability of liquid–liquid annular flows was studied both experimentally and numerically for horizontal and vertical configurations and for liquid pairs with different viscosities and densities. From stability analysis, it was found that if the annular flow has a negative perturbation growth rate, the system is stable to disturbances. Conversely, if the growth rate of the perturbation is positive, any small disturbances introduced into the system will grow in interfacial waves. For a large instability growth rate, breakup of the core is also possible, producing slug, plug, or dispersed flows. The instability growth rates are dependent on several factors, for example, the position of the interface with a thinner core resulting in a more unstable flow.

Although shear-thinning, shear-thickening, and Bingham fluids have all been considered to replace Newtonian fluids for liquid–liquid displacement,[3,31,58–69] the studies of viscoelastic liquids are few and usually the fluids combine both shear thinning and elastic properties (i.e., polymeric fluids).[70–78] For the case of the viscoelastic displaced phase, viscoelastic forces have shown to increase the amount of liquid left on the wall and lower the displacement efficiency. In contrast, Soares et al.[78] used a pure viscoelastic liquid (Boger fluid) as the displacing phase and found that with increasing flow rates, the displacement efficiency increased. Hue et al.[28] for a Boger fluid displacing phase showed that the remaining film close to the wall could be correlated with the Weissenberg number (Wi) of the displacing phase [the ratio of the fluid relaxation time to the characteristic flow time, $Wi = \lambda/(d/V)$, where λ is the viscoelastic fluid relaxation time, d is the channel diameter, and V is the superficial velocity]. The relaxation time of the displacing phase was also shown to influence the shape of the interfacial instabilities.

In this paper, the displacement of a Newtonian organic liquid by three Boger fluids with different relaxation times is studied experimentally and compared against the displacement by another Newtonian fluid. Characteristics of the interfacial instabilities, such as wave frequency, amplitude, and speed, are presented. It is shown that these properties are correlated with the elastic Mach number, highlighting the importance of elastic effects on the interfacial deformation. Based on these correlations, a modified empirical wave-based model is used to qualitatively describe the periodic interfacial instability appearing during the liquid displacement.

METHODOLOGY
Test liquids
Organic liquid (displaced phase)

A blend of 20 cP (SI20) and 100 cP (SI100) silicone oils (VWR Chemicals) is chosen as the displaced phase, allowing the viscosity of the displaced phase to change while the density and the interfacial tension are kept constant. Four different samples are produced, 90 wt. % SI20 and 10 wt. % SI100 with a viscosity of 23.86 cP (Org O), 73.5 wt. % SI20 and 26.5 wt. % SI100 with a viscosity of 32.52 cP (Org A), 72 wt. % SI20 and 28 wt. % SI100 with a viscosity of 33.79 cP (Org B), and 71 wt. % SI20 and 29 wt. % SI100 with a viscosity of 35.70 cP (Org C) (Table I). Viscosity data are obtained from rheological tests with a rotational rheometer (MCR 302, Anton Paar) equipped with 1° 50 mm diameter cone & plate geometry (CP50) and a Peltier plate set at 25 °C. The densities are measured using a pycnometer for ten different prepared samples, and an average value is used for each liquid (Table I). The refractive index is measured using an Abbe refractometer (Edmund Optics).

Aqueous liquid (displacing phase)

The displacing phase consists of an aqueous Newtonian liquid where different concentrations of long chain polymers are added to produce pure viscoelastic liquids. The Newtonian liquid (N) is made up of 20 wt. % polyethylene glycol (PEG, Sigma Alrich Science), 10 wt. % zinc chloride ($ZnCl_2$, Sigma Alrich Science), and 70 wt. % deionized (DI) water. One drop of black Nigrosin dye (Sigma Aldrich) is added per 10 ml of sample to differentiate the aqueous phase from the organic phase during imaging. This mixture composition is chosen to obtain refractive index equal to 1.390, which is similar to that of the organic phase (1.400) and the channel wall (1.404), thus preventing refractions during imaging. PEG is added to increase the viscosity of the aqueous phase. Rheological measurements confirmed that the liquid is Newtonian and has a constant viscosity equal to 19.68 cP. The interfacial tension between the organic and aqueous phases is in all cases equal to 26.08 mN/m, as measured with a force tensiometer

TABLE I. Summary of test liquid pairs and the physical properties for each liquid. The range of flow rates for each liquid pair is also given.

Fluid pair (displacing-displaced phase)	Fluid constituents	Density (kg/m³)	Density ratio (ρ_{aq}/ρ_{org})	Viscosity (cP)	Viscosity ratio (μ_{aq}/μ_{org})	Relaxation times (s)	Interfacial tension (mN/m)	Refractive index (—)	Flow rate range (ml/min)
N Aqueous-Org O	10 wt. % ZnCl₂ + 20 wt. % PEG + 70 wt. % DI water (N)	1089	1.15	19.677	0.82	-	26.08	1.40	0.025–0.40
	90 wt. % SI20 + 10 wt. % SI100	950		23.858				1.39	
Boger A-Org A	N + 500 ppm PEO 5 M	1090	1.15	26.685	0.82	(1) 0.063	26.08	1.40	0.025–0.30
	73.5 wt. % SI20 + 26.5 wt. % SI100	950		32.52				1.39	
Boger B-Org B	N + 700 ppm PEO 5 M	1091	1.15	27.807	0.82	(1) 0.099	26.08	1.40	0.05–0.27
	72 wt. % SI20 + 28 wt. % SI100	950		33.792		(2) 0.004		1.39	
Boger C-Org C	N + 1000 ppm PEO 5 M	1092	1.15	29.311	0.82	(1) 0.134	26.08	1.40	0.05–0.25
	71 wt. % SI20 + 29 wt. % SI100	950		35.701		(2) 0.020		1.39	

(K100c, Kruss GmbH) at 25 °C using a Wilhelmy plate attachment (Table I).

To produce the Boger fluids, small amounts of polyethylene oxide (Sigma Alrich Science) with a molecular weight of 5 000 000 Da (5 M PEO) are added to the Newtonian liquid. Three samples of Boger fluid are prepared by adding 500 ppm (Boger A), 700 ppm (Boger B), and 1000 ppm (Boger C) of 5 M PEO to the Newtonian liquid. Small amplitude oscillatory shear (SAOS) at a 1% strain with angular frequencies between 0.1 and 400 rad/s is used to measure the storage and loss moduli (G' and G'') of the samples, and the relaxation times are obtained from the crossings of the G' and G'' curves.[79,80] The SAOS methodology is used instead of the normal stress difference method as the solutions have low viscosity and the first normal stress difference is below the sensitivity of the rheometer (0.001 Pa). Boger A has a polymer concentration at the limit of the critical value for a dilute solution, and its elasticity is characterized by a single relaxation time at 0.063 s. The other two solutions, Boger B and Boger C, have polymer concentrations that are in the semi-dilute region and exhibit multiple relaxation times. Both Boger B and Boger C have two distinct relaxation times, Boger B at 0.099 and 0.004 s and Boger C at 0.13 and 0.02 s (Table I). The presence of short chain PEG in the Newtonian fluid suppresses the entanglement and sliding of the long chain PEO, preventing any shear-thinning effects.[79] The detailed methodology for preparing the sample liquids can be found in Hue et al.[28]

By changing the viscosity of the organic phase, the viscosity ratio of the liquid pairs is kept constant at 0.82. The density ratio is also constant for each liquid pair at 1.15. Hence, the only appreciable difference between each liquid pair is the elasticity of the displacing phase, expressed as the viscoelastic relaxation time of the liquid.

Experimental setup

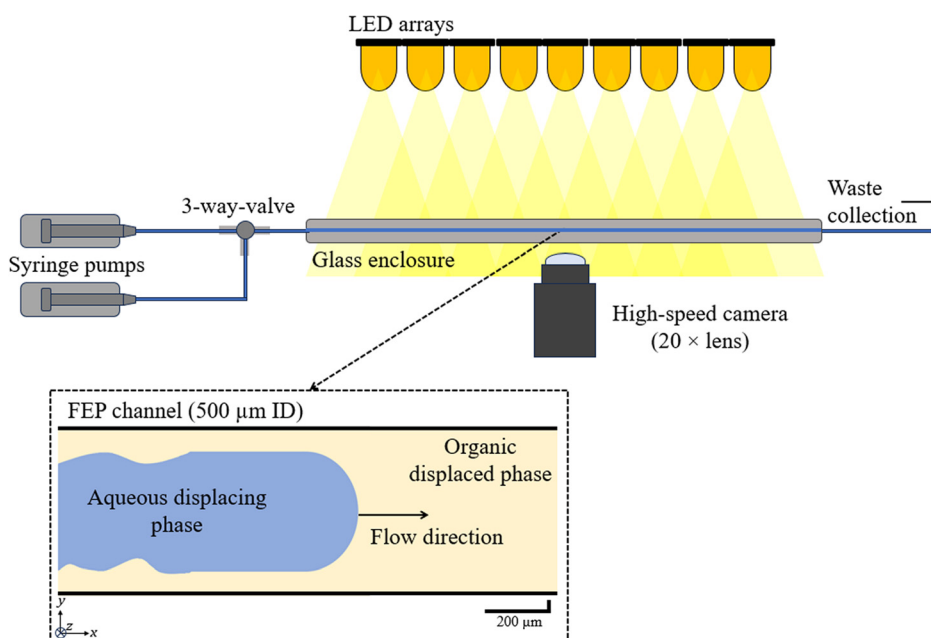A bright field shadowgraphy setup is used to obtain planar images of the displacement core, using a high-speed camera (Phantom V1212, Vision Research, Ametek) with a 20 × microscopic lens (depth of field, 1.60 μm, Mitutoyo) and non-flickering light emitting diode (LED) backlights (GS Vitec). The channel is a circular hydrophobic fluorinated ethylene–propylene (FEP) capillary (Dolomite, Unchained Labs) with an internal diameter (ID) of 500 μm and a total length of 30 cm. The channel is placed inside a rectangular enclosure filled with a 56% glycerol–water solution to match the refractive index of the wall and avoid any curvature effects (Fig. 1).

Experimental procedure

The channel is first flooded with the displaced phase, and a three-way valve is used to switch between the displaced and the displacing phase to allow for a seamless transition without introducing any air bubbles. The channels from the syringes leading up to the main channel as well as the ports in the three-way valve have the same ID as the main channel, which is equal to 500 μm. The focal plane of the lens is set at the middle of the channel and the camera is fixed at 10 cm from the channel inlet to avoid any end effects.[81] The resulting displacement core is recorded on an x–y plane at frame rates between 1000 and 5000, depending on the flow rate, for a minimum of 15 s up to 120 s, capturing both the displacement front and the instabilities along the interface. A syringe pump (KD Scientific) is used to deliver both fluids, with the displacing flow rates varying between 0.025–0.40 ml/min and 0.05 and 0.25 ml/min for the lowest and the highest viscosities of the displacing phase, respectively; these values are within the highest pressure that the pump could deliver.

Post-processing procedure

An example of the interface tracking procedure is shown in Fig. 2(a). The position of the interface between the displacing and the displaced phases is tracked at a single x-position [shown as a red dashed line X–X in Fig. 2(a)] over time using an in-house algorithm

FIG. 1. Schematic of the experimental and bright field shadowgraphy setup. The light source, the glass enclosure containing the channel, and the camera are placed in parallel. Inset: Schematic of the liquid–liquid displacement in a channel, with the displaced phase in yellow, and the displacing phase in blue. In the planar coordinates, flow is in the x-direction, while the recorded interface varies in the y-direction.
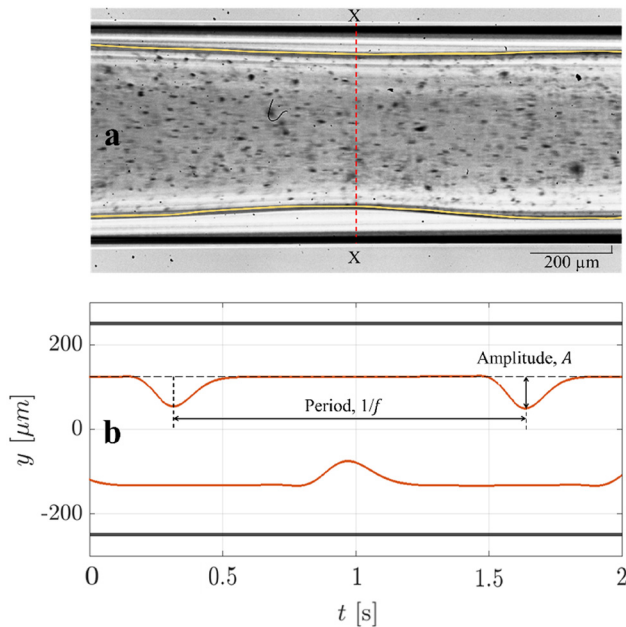
FIG. 2. (a) Detected interface (yellow) overlaid onto an original image captured during an interfacial instability. The red dashed line X–X shows the locations where the upper and the lower interface positions are recorded for each frame over time. (b) Spatial–temporal plot of the tracked interface with the definitions of the interface period and amplitude shown. The results are for the displacement of Boger A-Org A at 0.15 ml/min.

on MATLAB 2020a (MathWorks). The resulting measurements are a spatial temporal plot of the interface position; an example of the interface data over time is shown in Fig. 2(b). Full details of the tracking algorithm used can be found in Hue *et al.*[28]

From Fig. 2(b), the interface amplitude, *A*, is calculated from the distance of the peaks from the base of the wave. The wave frequency, *f*, is estimated from the fast Fourier transform of the interface signal. The wave velocity, V_{wave}, is measured by recording the distance a wave peak has traveled over 50 frames. For each of the wave properties, at least 20 measurements are averaged and maximum deviations of 9.8% for the wave amplitude, 2% for the frequency, and 12.5% for the wave velocity were found.

RESULTS

Figure 3 shows an example of the top and bottom interface data for the Newtonian fluid displacement case and a Boger fluid displacement case at two different flow rates. For the same flow rate, the N–N case [Fig. 3(a)] shows a disturbed interface, which results from the differences in the viscosities and densities of the two phases. In contrast, the displacement with the Boger fluid [Figs. 3(b) and 3(c)] exhibits a periodic interfacial deformation, which is attributed to the propagation of elastic instabilities in the viscoelastic fluid. The characteristic time of the flow ($\tau = d/V$, where *d* is the channel diameter and *V* is the superficial velocity) ranges between 0.011 and 0.23 s for the lowest and the highest flow rates for all cases. The values are comparable to the relaxation times of the Boger fluids (0.06, 0.09, and 0.13 s), suggesting that both viscous and elastic effects are important in the displacement flow.

The curvature of the local streamlines in the flow causes the polymer chains in the Boger fluid to stretch, thereby increasing the local elastic normal stresses, which trigger the elastic waves;[82–85] these are the sources of the instabilities manifested as interfacial waves. The small disturbances seen in the N–N flow are suppressed by the Boger fluid, as the energies are absorbed and redistributed into the polymers.

In Figs. 3(b) and 3(c), as the Boger fluid flow rate increases to 0.3 ml/min from 0.1 ml/min, the frequency of the waves increases.

The section "Wave properties" will discuss the periodic instability obtained with different Boger displacing liquids, including the amplitude, the frequency, the wave velocity, and the phase difference between the top and the bottom parts of the interface. For the current channel and ranges of flow rates, the flow is laminar with the Reynolds number ($Re = \rho V d/\mu$, where ρ is the density of the displacing phase, *V* is the superficial velocity, *d* is the channel diameter, and μ is the viscosity of the displacing phase) below one in all cases. Similarly, the Bond number [$Bo = \Delta \rho d^2 g/\sigma$, where $\Delta \rho$ is the density difference between the two phases ($\Delta \rho = \rho_{aq} - \rho_{org}$, with subscripts *aq* and *org* representing the aqueous and the organic phases, respectively), g is the gravitational acceleration and σ is the interfacial tension] is below one, and the effect of gravity can be neglected.

Wave properties

The amplitudes of both the top and bottom interfaces for increasing flow rates are shown in Fig. 4(a) for the three cases of Boger fluids. For all Boger fluids, the amplitude increases linearly with the flow rate until a maximum is reached, before decreasing again. In addition, the amplitude increases as the relaxation time of the Boger fluid decreases. Indeed, Boger A shows a maximum amplitude of 50 μm, while Boger fluids B and C show, respectively, a maximum amplitude of 35 and 22 μm.

At low flow rates (below 0.1 ml/min), the Weissenberg number is small ($Wi < 1$), and the elastic effect of the polymer on the flow is weak. The amplitude increases with the displacing phase flow rate due to the non-linear response of the elastic stress with increasing flow rate. For flow rates above 0.12, 0.10, and 0.08 ml/min for Boger A, Boger B, and Boger C, respectively, the amplitude decreases with an increasing flow rate. For these configurations, the elastic effects should be strong (with a transition toward elastic turbulence for $Wi > 1$[86]). At this regime, the attenuation from polymer relaxation and viscous dissipation[87–89] is expected to increase with the flow rate, which confirm the experimental observations.

At even higher flow rates, beyond the values measured in this study, inertial effects are expected to dominate and the wave amplitudes will start increasing again.[56,90,91] Driel and Ayyash[92] showed in their study, for a laminar flow of a viscoelastic fluid with forced oscillation at the inlet, that there is an initial increase in the amplitude up to a maximum value before it decreased again. Additionally, by increasing the polymer concentration and consequently the relaxation time of the displacing phase, the perturbation growth rate decreases, resulting in smaller wave amplitudes for the same displacing flow rates.[93]

Figure 4(b) shows the wave amplitude normalized by the maximum amplitude A_{max} (see the Appendix) against the elastic Mach number (*Ma*), which accounts for the elastic, viscous, and inertial forces, and can be defined as a combination of the Weissenberg number (*Wi*) and the Reynolds number (*Re*) as follows:[94–96]
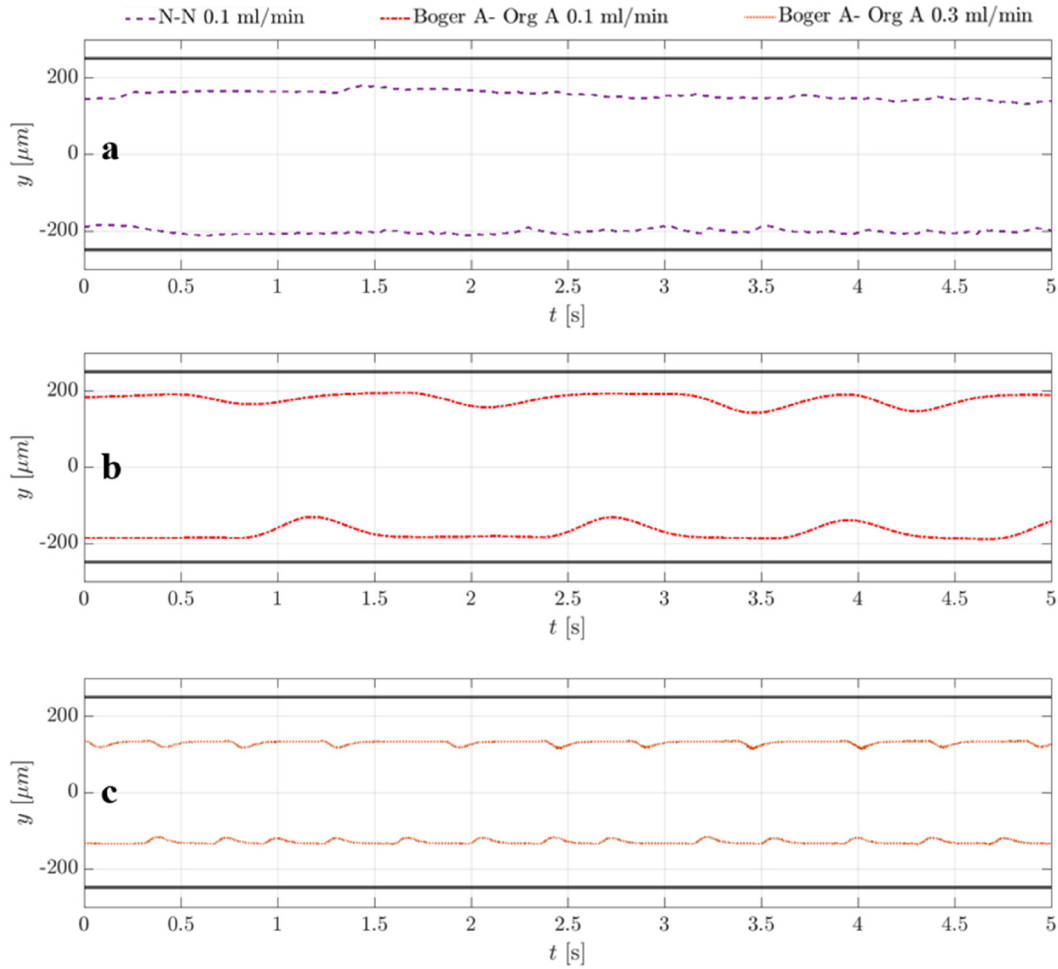
FIG. 3. Interfacial data for (a) N-Org O displacement at 0.1 ml/min, (b) Boger A-Org A displacement at 0.1 ml/min, and (c) Boger A-Org A displacement at 0.3 ml/min. The two lines in each graph represent the top and the bottom interfaces captured by the camera. Black borders indicate the position of the channel wall.

$$Ma = \sqrt{Wi\,Re} \equiv V/\sqrt{\mu/\lambda\rho}, \qquad (1)$$

where V is the superficial velocity, μ is the steady shear viscosity, ρ is the density, and λ is the largest viscoelastic relaxation time of the displacing phase. The term $\sqrt{\mu/\lambda\rho}$ is further defined as the elastic wave speed of the viscoelastic liquid, which is a measure of the propagation speed of the elastic stress within the fluid. The elastic wave speed is an inherent fluid property, which does not change with the flow conditions.

As can be seen in Fig. 4(b), the data collapses into two lines before and after $Ma = 0.5$. Following the previous assumption that the change of slope comes with the appearance of elastic turbulence, Ma can be chosen as a predicator of elastic turbulence for the present microsystem. For $Ma < 0.5$, the dimensionless amplitude increases with Ma due to the increase in elastic stress propagating larger waves. For $Ma > 0.5$, the normalized amplitude decreases with Ma and the interfacial waves are attenuated at a rate faster than the increase in elastic stress because the energy is redistributed from the interface to the bulk of the flow by elastic turbulence. The following linear empirical correlations were found to describe the non-dimensional amplitudes:

$$A/A_{\max} = \begin{cases} 2.1\,Ma, & Ma < 0.5, \\ -0.65\,Ma + 1.33, & Ma > 0.5. \end{cases} \qquad (2)$$

The first part of Eq. (2) has an R^2 value of 0.93, while the second part has an R^2 value of 0.95.

Contrary to the wave amplitude, the frequency shows a monotonic increase with flow rates [Fig. 5(a)]. The frequencies are similar for all Boger fluids at low flow rates, while for flow rates above 0.15 ml/min, Boger A, the fluid with the lowest viscoelastic relaxation time exhibits higher frequencies compared to the other two. The wave frequency, normalized with the viscoelastic relaxation time, is plotted against the Ma in Fig. 5(b). The dimensionless frequency collapses into a single curve for all cases, and the following empirical correlation describes the data with an R^2 value of 0.97

$$\lambda.f = 0.115\,Ma^{3/2}. \qquad (3)$$

Meanwhile, Fig. 6(a) shows that the wave velocity increases with the displacing phase flow rate, similar to the behavior of the wave
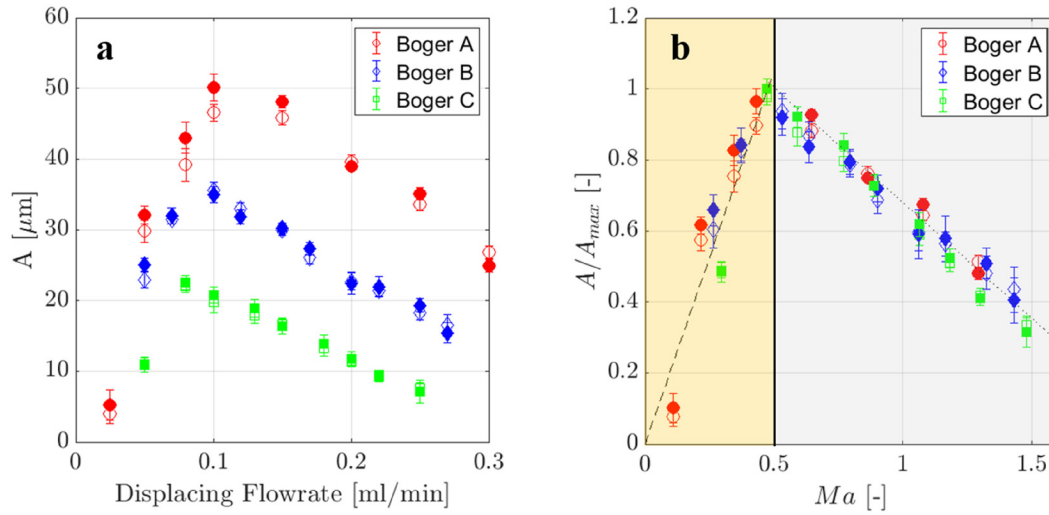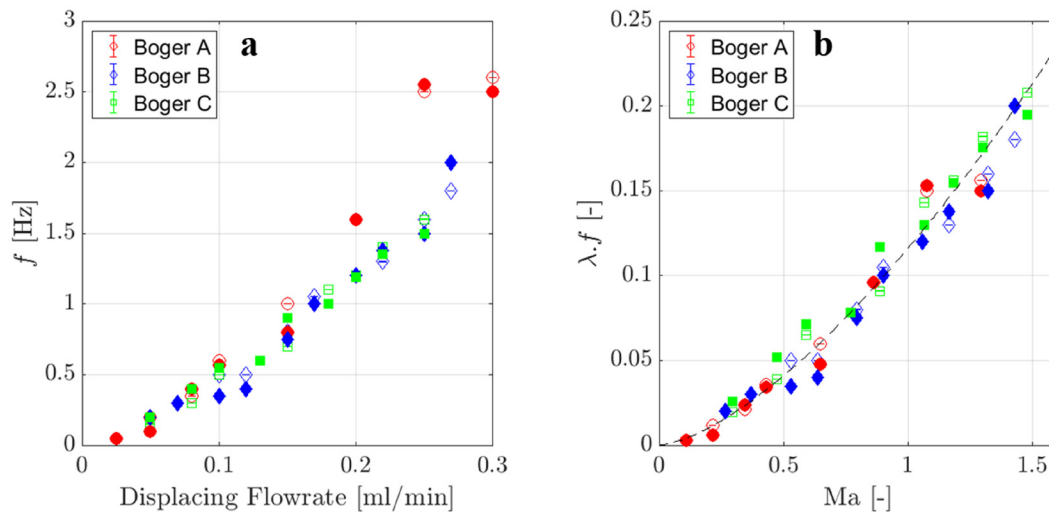
FIG. 4. (a) Interfacial instability amplitude A against the displacing phase flow rate for the three different Boger fluids. (b) Dimensionless interfacial instability amplitude against the elastic Mach number for the three different Boger fluids. The yellow shaded region shows the first part of Eq. (2) (dashed line), and the gray shaded region shows the second part of Eq. (2) (dotted line). Open symbols are amplitude measurements from the top interface, and closed symbols are amplitude measurements from the bottom interface.

frequency. At low flow rates, all fluids show similar wave velocities, while at high flow rates, the wave velocity slightly decreases with an increasing viscoelastic relaxation time.

The wave velocity, normalized with the viscoelastic relaxation time and the channel diameter, reduces to a line when plotted against Ma, as shown in Fig. 6(b). The dimensionless wave velocities can be described by Eq. (4) [dashed line in Fig. 6(b)], with an R^2 value of 0.96

$$V_{wave} \cdot \left(\frac{\lambda}{d}\right) = 0.1\, Ma. \tag{4}$$

In contrast to the wave amplitude, which initially increases and then decreases with increasing Ma, both the wave frequency and the wave velocity increase monotonically with Ma. The changes in amplitude are attributed to the force balance normal to the interface; an increase in Ma increases the elastic stress normal to the interface. However, as discussed above, at Ma above 0.5, there is a transition to the elastic turbulence even though the Reynolds number remains low ($Re < 1$). The energy at the interface from the elastic stress is redistributed to the bulk of the flow and hence the amplitude of the interface decreases. Meanwhile, the frequencies and velocities of the interfacial

FIG. 5. (a) Frequency of instability waves f against the displacing phase flow rate for the three different Boger fluids. (b) Dimensionless frequency against the elastic Mach number for the three different Boger fluids. The empirical correlation [Eq. (3)] is shown as a black dashed line. Open symbols are frequency measurements from the top interface, and closed symbols are frequency measurements from the bottom interface.
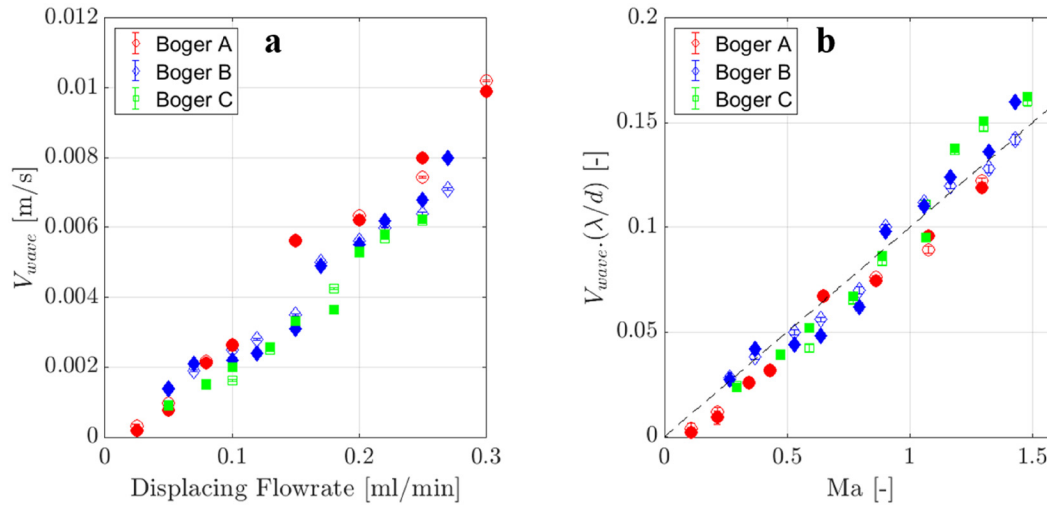
FIG. 6. (a) Wave velocity V_{wave} against the displacing phase flow rate for the three different Boger fluids. (b) Dimensionless wave velocities against the elastic Mach number for the three different Boger fluids. The empirical correlation [Eq. (4)] is shown as a black dashed line. Open symbols are the wave velocity measurements from the top interface, and closed symbols are the wave velocity measurements from the bottom interface.

waves are less strongly dependent on the normal forces at the interface. Instead, the propagation of waves in the direction of flow is related to the velocity of the displacing phase. Similar trends for the frequency and the wave velocity were also observed for viscoelastic flows past cylinders by Varshney and Steinberg,[87] who found that these wave properties increased with the flow rate of the viscoelastic fluid.

Phase difference

The wave properties between the top and the bottom interfaces discussed in the section "Wave properties" are very similar. However, it was found that the bottom interface is delayed compared to the top interface as can be seen in Fig. 7 for Boger A-Org A displacement at 0.35 ml/min. For all cases, the average phase difference between the top and the bottom interfaces was found to be around π, or half the period of oscillation, with an average error of 3.8%, as shown in Fig. 8. As the displacing phase core is three-dimensional, the phase shift between the measured top and bottom interfaces is expected since the images are captured on a two-dimensional plane. The shape of the

core with the constant phase difference of π will be discussed in detail in the section "Extension of planar waves as a representation of 3D waves."

Empirical plane wave modeling

Assuming that a single point on the interface during displacement follows a sinusoidal deformation over time, the interface can be described by

$$x(t) = A\sin(\omega t + \varphi), \tag{5}$$

where x is the instantaneous position of the interface, A is the peak amplitude, ω is the radian frequency ($\omega = 2\pi f$, f is the interfacial wave frequency), t is the instantaneous time, and φ is the phase of the wave.

However, experimental observations showed that the interfacial deformation is more similar to a half rectified sinusoidal wave, which can be obtained by multiplying Eq. (5) with $\frac{1}{2}[\text{sgn}(\sin(\omega t + \varphi)) + 1]$, where sgn represents a sign function. Additionally, as previously
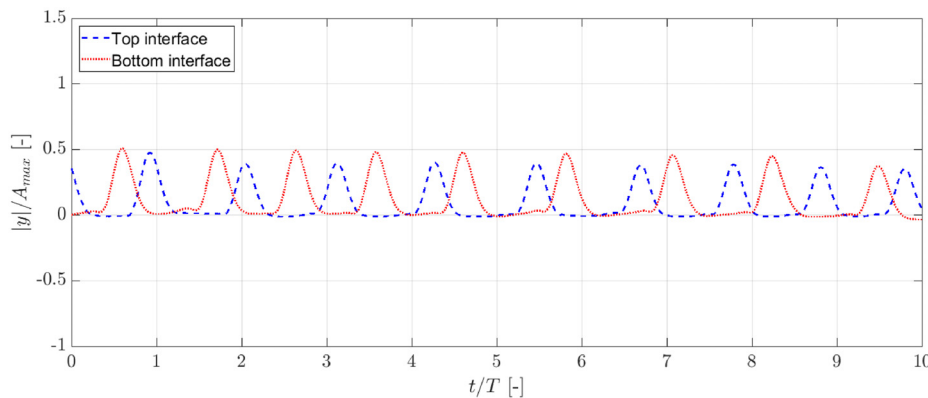
FIG. 7. The top and the bottom interfaces overlaid onto each other for Boger A-Org A displacement at 0.35 ml/min. The y-position of the interface is normalized with the maximum amplitude, and the experimental time is normalized with the period of oscillation.
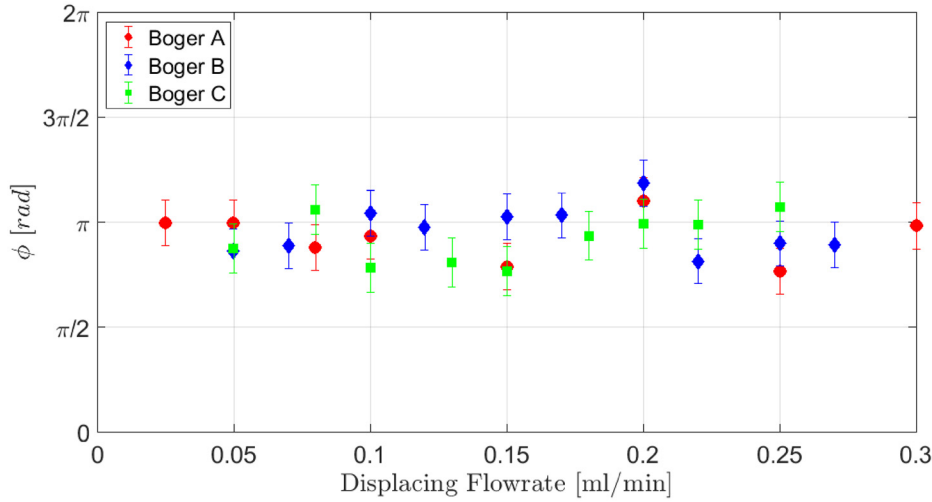
FIG. 8. Phase difference between the top and the bottom interfaces for the three different Boger fluids.

shown, the top and the bottom interfaces follow mostly the same pattern with a phase shift, ϕ, between them. To obtain the mean position of the interface relative to the channel wall, the correlation for the empirical film thickness, H, by Hue *et al.*[28] is used. Applying these to Eq. (5) yields

$$x(t) = \begin{cases} \frac{1}{2}\left[sgn(\sin(\omega t + \varphi)) + 1\right].A\sin(\omega t + \varphi) + H, \\ \quad Top\ interface, \\ \frac{1}{2}\left[sgn(\sin(\omega t + \varphi + \phi)) + 1\right].A\sin(\omega t + \varphi + \phi) - H, \\ \quad Bottom\ interface. \end{cases}$$

(6)

The key instability parameters obtained previously for the Boger fluids [Eqs. (2)–(4)] can be used to build a toy model based on Eq. (6). Comparisons between this empirical model and an independent experiment of Boger A-Org A displacement at a flow rate of 0.35 ml/min in Fig. 9 showed good agreement. Qualitatively, the empirical model agrees well with experimental data, with very small deviations appearing in both the frequency and the amplitude. In fact, when comparing the interface position between the model and the experimental data, a

mean absolute percentage error (MAPE) of 4.60% and 4.36% is obtained for the top and the bottom interfaces, respectively, indicating a good fit. The MAPE is defined by

$$MAPE = \frac{1}{n}\sum_{1}^{n}\left|\frac{x_{exp} - x_{model}}{x_{exp}}\right|,$$

(7)

where n is the number of data points, x_{exp} is the position of the interface measured from experiments, and x_{model} is the interface position from the planar wave model.

The mean position of the interface obtained experimentally is not constant. Instead, the interface moves closer to the channel wall with time as the displaced phase is removed from the channel. This results in an increase in the deviations between experiments and model with time.

Extension of planar waves as a representation of 3D waves

As discussed above, the top and the bottom interfaces display the same average wave properties for each case (see Figs. 4–6). Assuming continuity of the interface along the channel, a helical deformation, similar to a coiled structure, is expected.[97] Indeed, this wave shape has
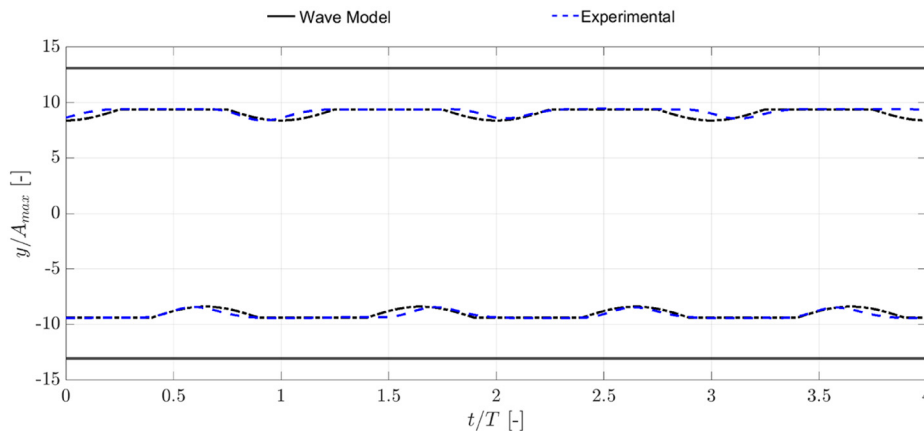

FIG. 9. Dimensionless interface position against dimensionless time for the interface between the proposed empirical wave model in a black dotted line [Eq. (6)] and the experimental measurements in a blue dashed line for the Boger A-Org A displacement at 0.35 ml/min. The two lines in each graph represent the top and the bottom interfaces, and the black borders indicate the position of the channel wall. The y-position of the interface is normalized with the maximum amplitude, and the experimental time is normalized with the period of oscillation.
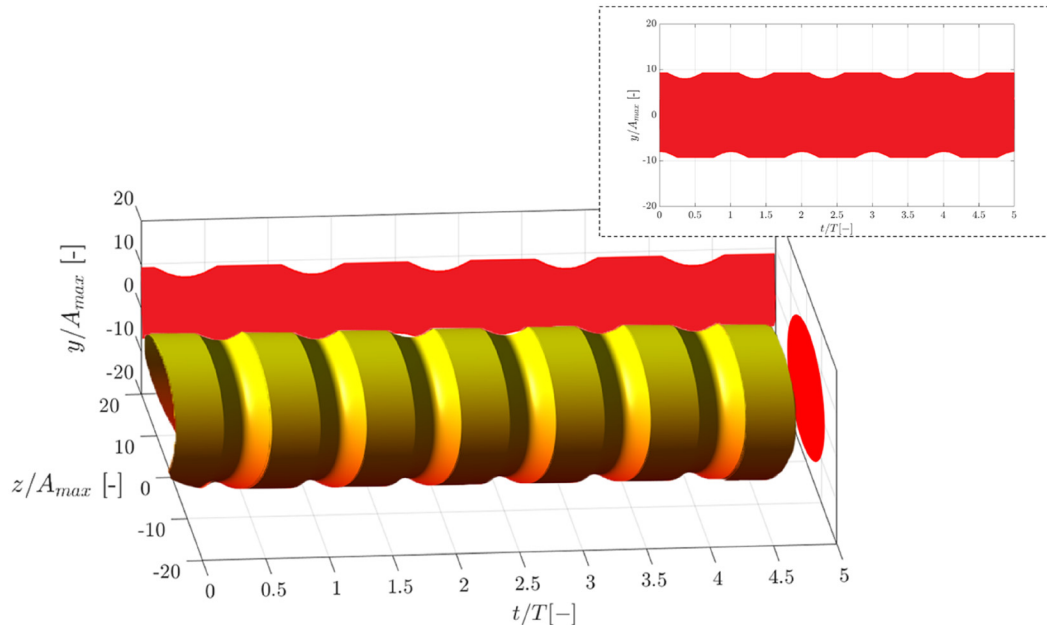
FIG. 10. 3D model of helical screw waves, produced using Eq. (6). The projection of the 3D waves on a plane is shown on the back and as an image inset. The cross section of the waves is shown on the right. The interface is normalized with the maximum amplitude, and the experimental time is normalized against the period of oscillation.

been observed in previous literature findings in large channels for unstable annular flows.[53,57] By generating a volume of revolution from the plane wave model [Eq. (6)], a 3D representation of the wave is produced, showing a helical structure (Fig. 10). The planar projection of this 3D wave, shown in red in Fig. 10, illustrates a 2D wavy interface similar to the one observed experimentally. Additionally, the cross-sectional shape of the 3D wave is found to be circular, which is consistent with the shape of the viscous finger inside a circular channel during displacement.[15]

CONCLUSIONS

The displacement of a Newtonian organic liquid by viscoelastic Boger liquids with different relaxation times was studied. It was found that while for a Newtonian displacing fluid the interface had small irregular waves, when the viscoelastic fluids were used, the instabilities became periodic and the amplitudes increased. The amplitudes presented an interesting trend, increasing initially with the flow rate and then decreasing. This behavior was attributed to the relative importance of the elastic effects on the flow. The frequency and the velocity of the instability waves both increased with increasing displacement flow rates. It was possible to correlate all three dimensionless wave characteristics, amplitude, frequency, and wave velocity, with an elastic Mach number, Ma, defined as the ratio of the flow velocity with the elastic wave propagation velocity. The wave properties of both the top and the bottom interfaces obtained from the planar images of the displacement agreed well with a phase shift between them equal to half an oscillation period. Using the wave properties and the phase shift, it was possible to reconstruct the three-dimensional waves, which resembled a helical screw structure.

In the future, it is planned to investigate the flow fields during the interfacial instability. Using particle image velocimetry (PIV) and particle tracking velocimetry (PTV) techniques, the velocity fields close to the interfacial instability in both phases can be measured, which might reveal any non-uniform structures in the flow.

AUTHOR DECLARATIONS
Conflict of Interest

The authors have no conflicts to disclose.

Author Contributions

Seng Hoe Hue: Conceptualization (equal); Data curation (equal); Formal analysis (equal); Investigation (equal); Methodology (equal); Validation (equal); Visualization (equal); Writing – original draft (equal); Writing – review & editing (equal). **Loïc Chagot:** Formal analysis (equal); Supervision (equal); Validation (equal); Writing – review & editing (equal). **Panagiota Angeli:** Conceptualization (equal); Funding acquisition (equal); Resources (equal); Supervision (equal); Writing – review & editing (equal).

DATA AVAILABILITY

The data that support the findings of this study are available from the corresponding author upon reasonable request.
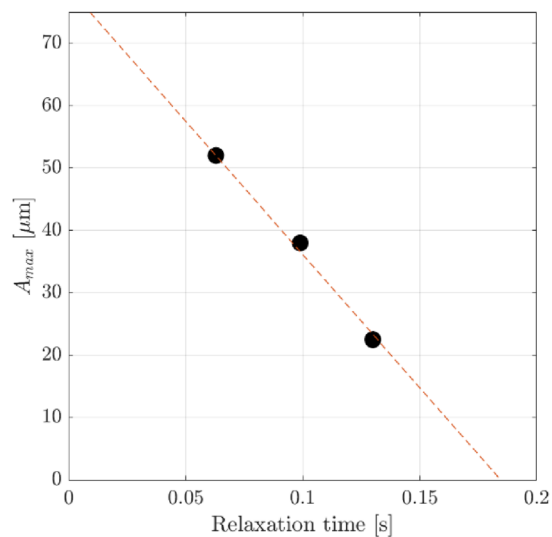
FIG. 11. Maximum amplitude vs relaxation time of the displacing phase.

APPENDIX: MAXIMUM AMPLITUDE AND RELAXATION TIME DEPENDENCY

　　　Figure 11 shows the dependence of the maximum amplitude on the physical property of the fluid through its linear relationship with the viscoelastic relaxation time of the displacing phase.

REFERENCES

[1]A. S. Hanamertani, R. M. Pilus, and S. Irawan, in *ICIPEG 2016* (Springer, 2017), pp. 133–147.

[2]O. Massarweh and A. S. Abushaikha, "The use of surfactants in enhanced oil recovery: A review of recent advances," Energy Rep. **6**, 3150–3178 (2020).

[3]R. Mahon, G. Oluyemi, B. Oyeneyin, and Y. Balogun, "Experimental investigation of the displacement flow mechanism and oil recovery in primary polymer flood operations," SN Appl. Sci. **3**(5), 557 (2021).

[4]M. Hashimoto, P. Garstecki, H. A. Stone, and G. M. Whitesides, "Interfacial instabilities in a microfluidic Hele-Shaw cell," Soft Matter **4**(7), 1403–1413 (2008).

[5]I. Shukla, N. Kofman, G. Balestra, L. Zhu, and F. Gallaire, "Film thickness distribution in gravity-driven pancake-shaped droplets rising in a Hele-Shaw cell," J. Fluid Mech. **874**, 1021–1040 (2019).

[6]P. G. Saffman and G. Taylor, "The penetration of a fluid into a porous medium or Hele-Shaw cell containing a more viscous liquid," Proc. R. Soc. London, Ser. A **245**, 312–329 (1958).

[7]J. Avendaño, N. Lima, A. Quevedo, and M. Carvalho, "Effect of surface wettability on immiscible displacement in a microfluidic porous media," Energies **12**(4), 664 (2019).

[8]D. Kawale, E. Marques, P. L. J. Zitha, M. T. Kreutzer, W. R. Rossen, and P. E. Boukany, "Elastic instabilities during the flow of hydrolyzed polyacrylamide solution in porous media: Effect of pore-shape and salt," Soft Matter **13**(4), 765–775 (2017).

[9]H. S. Rabbani, D. Or, Y. Liu, C.-Y. Lai, N. B. Lu, S. S. Datta, H. A. Stone, and N. Shokri, "Suppressing viscous fingering in structured porous media," Proc. Natl. Acad. Sci. U. S. A. **115**(19), 4833–4838 (2018).

[10]Y. Shi and G. H. Tang, "Non-Newtonian rheology property for two-phase flow on fingering phenomenon in porous media using the lattice Boltzmann method," J. Non-Newtonian Fluid Mech. **229**, 86–95 (2016).

[11]H. Shokri, M. H. Kayhani, and M. Norouzi, "Saffman–Taylor instability of viscoelastic fluids in anisotropic porous media," Int. J. Mech. Sci. **135**, 1–13 (2018).

[12]K. Singh, M. Jung, M. Brinkmann, and R. Seemann, "Capillary-dominated fluid displacement in porous media," Annu. Rev. Fluid Mech. **51**, 429–449 (2019).

[13]Y. Han and N. Shikazono, "Measurement of liquid film thickness in micro square channel," Int. J. Multiphase Flow **35**(10), 896–903 (2009).

[14]Y. Lu, N. M. Kovalchuk, and M. J. H. Simmons, "Residual film thickness following immiscible fluid displacement in noncircular microchannels at large capillary number," AIChE J. **64**(9), 3456–3466 (2018).

[15]Y. Lu, N. M. Kovalchuk, Z. Che, and M. J. H. Simmons, "Interfacial instabilities due to immiscible fluid displacement in circular and non-circular microchannels," Exp. Therm. Fluid Sci. **113**, 110045 (2020).

[16]Y. Liu, A. Hansen, E. Block, N. R. Morrow, J. Squier, and J. Oakey, "Two-phase displacements in microchannels of triangular cross-section," J. Colloid Interface Sci. **507**, 234–241 (2017).

[17]B. Bera, I. Hauner, M. Qazi, D. Bonn, and N. Shahidzadeh, "Oil-water displacements in rough microchannels," Phys. Fluids **30**(11), 112101 (2018).

[18]D. Li, R. Yang, H. Cao, F. Yao, C. Shen, C. Zhang, and S. Wu, "Experimental study on gas flow in a rough microchannel," Front. Energy Res. **10**, 863733 (2022).

[19]D. Yang, M. Krasowska, C. Priest, and J. Ralston, "Dynamics of capillary-driven liquid-liquid displacement in open microchannels," Phys. Chem. Chem. Phys. **16**(44), 24473–24478 (2014).

[20]P. Aussillous and D. Quere, "Quick deposition of a fluid on the wall of a tube," Phys. Fluids **12**(10), 2367–2371 (2000).

[21]F. P. Bretherton, "The motion of long bubbles in tubes," J. Fluid Mech. **10**(2), 166–188 (1961).

[22]F. Fairbrother and A. E. Stubbs, "Studies in electro-endosmosis. Part VI. The 'bubble-tube' method of measurement," J. Chem. Soc. **1935**, 527.

[23]S. Irandoust and B. Andersson, "Liquid film in Taylor flow through a capillary," Ind. Eng. Chem. Res. **28**, 1684–1688 (1989).

[24]Y. Han and N. Shikazono, "Measurement of the liquid film thickness in micro tube slug flow," Int. J. Heat Fluid Flow **30**(5), 842–853 (2009).

[25]R. N. Marchessault and S. G. Mason, "Flow of entrapped bubbles through a capillary," Ind. Eng. Chem. **52**(1), 79–84 (1960).

[26]G. I. Taylor, "Deposition of a viscous fluid on the wall of a tube," J. Fluid Mech. **10**(2), 161–165 (1961).

[27]G. Balestra, L. Zhu, and F. Gallaire, "Viscous Taylor droplets in axisymmetric and planar tubes: From Bretherton's theory to empirical models," Microfluid. Nanofluid. **22**, 67 (2018).

[28]S. H. Hue, L. Chagot, and P. Angeli, "Viscoelastic effects of immiscible liquid–liquid displacement in microchannels with bends," Phys. Fluids **34**(7), 073111 (2022).

[29]E. J. Soares, R. L. Thompson, and D. C. Niero, "Immiscible liquid-liquid pressure-driven flow in capillary tubes: Experimental results and numerical comparison," Phys. Fluids **27**(8), 082105 (2015).

[30]E. J. Soares and R. L. Thompson, "Flow regimes for the immiscible liquid-liquid displacement in capillary tubes with complete wetting of the displaced liquid," J. Fluid Mech. **641**, 63–84 (2009).

[31]M. A. Tehrani, S. H. Bittleston, and P. J. G. Long, "Flow instabilities during annular displacement of one non-Newtonian fluid by another," Exp. Fluids **14**(5), 246–256 (1993).

[32]M. K. Smith, "The mechanism for the long-wave instability in thin liquid films," J. Fluid Mech. **217**, 469–485 (1990).

[33]P. A. M. Boomkamp and R. H. M. Miesen, "Classification of instabilities in parallel two-phase flow," Int. J. Multiphase Flow **22**, 67–88 (1996).

[34]R. Balasubramaniam, N. Rashidnia, T. Maxworthy, and J. Kuang, "Instability of miscible interfaces in a cylindrical tube," Phys. Fluids **17**(5), 052103 (2005).

[35]C. Y. Chen and E. Meiburg, "Miscible displacements in capillary tubes. Part 2. Numerical simulations," J. Fluid Mech. **326**, 57–90 (1996).

[36]R. Hu, J. Wan, Z. Yang, Y. F. Chen, and T. Tokunaga, "Wettability and flow rate impacts on immiscible displacement: A theoretical model," Geophys. Res. Lett. **45**(7), 3077–3086, https://doi.org/10.1002/2017GL076600 (2018).

[37]J. Kuang, T. Maxworthy, and P. Petitjeans, "Miscible displacements between silicone oils in capillary tubes," Eur. J. Mech. B **22**(3), 271–277 (2003).

[38]L. Yu and S. J. H. Mark, in 9th International Conference on Multiphase Flow, Firenze, Italy, May 22–27, 2016.

[39]B. K. Moore, D. G. Pahinkar, and S. Garimella, "Experimental and analytical investigation of displacement flows in microchannels," Int. J. Heat Mass Transfer **112**, 745–757 (2017).

[40]P. Petitjeans and T. Maxworthy, "Miscible displacements in capillary tubes. Part 1. Experiments," J. Fluid Mech. **326**, 37–56 (1996).

[41]K. C. Sahu, H. Ding, P. Valluri, and K. O. Matar, "Pressure-driven miscible two-fluid channel flow with density gradients," Phys. Fluids **21**(4), 043603 (2009).

[42]J. Scoffoni, E. Lajeunesse, and G. M. Homsy, "Interface instabilities during displacements of two miscible fluids in a vertical pipe," Phys. Fluids **13**(3), 553–554 (2001).

[43]A. A. Velizhanin and O. A. Simonov, AIP Conf. Proc. **1893**, 030075 (2017).

[44]E. J. Soares, M. S. Carvalho, and P. R. Souza Mendes, "Immiscible liquid-liquid displacement in capillary tubes," J. Fluids Eng. **127**(1), 24–31 (2005).

[45]R. Govindarajan and K. C. Sahu, "Instabilities in viscosity-stratified flow," Annu. Rev. Fluid Mech. **46**, 331–353 (2014).

[46]R. W. Aul and W. L. Olbricht, "Stability of a thin annular film in pressure-driven, low-Reynolds-number flow through a capillary," J. Fluid Mech. **215**, 585–599 (1990).

[47]Y. Cao and R. Li, "A liquid plug moving in an annular pipe—Flow analysis," Phys. Fluids **30**(9), 093605 (2018).

[48]H. Foroughi, A. Abbasi, K. S. Das, and M. Kawaji, "Immiscible displacement of oil by water in a microchannel: Asymmetric flow behavior and nonlinear stability analysis of core-annular flow," Phys. Rev. **85**(2), 026309 (2012).

[49]H. Foroughi and M. Kawaji, "Viscous oil-water flows in a microchannel initially saturated with oil: Flow patterns and pressure drop characteristics," Int. J. Multiphase Flow **37**(9), 1147–1155 (2011).

[50]G. Ooms, C. Vuik, and P. Poesio, "Core-annular flow through a horizontal pipe: Hydrodynamic counterbalancing of buoyancy force on core," Phys. Fluids **19**(9), 092103 (2007).

[51]G. Ooms and P. Poesio, "Stationary core-annular flow through a horizontal pipe," Phys. Rev. E **68**(6), 066301 (2003).

[52]D. Salin and L. Talon, "Revisiting the linear stability analysis and absolute-convective transition of two fluid core annular flow," J. Fluid Mech. **865**, 743–761 (2019).

[53]R. Bai, K. Chen, and D. D. Joseph, "Lubricated pipelining: Stability of core—Annular flow. Part 5. Experiments and comparison with theory," J. Fluid Mech. **240**, 97–132 (1992).

[54]H. H. Hu and D. D. Joseph, "Lubricated pipelining: Stability of core-annular flow. Part 2," J. Fluid Mech. **205**, 359–396 (1989).

[55]D. D. Joseph, "Lubricated pipelining: Stability of core-annular flow. Part 4. Ginzburg-Landau equations," J. Fluid Mech. **227**, 587–615 (1991).

[56]L. Preziosi, K. Chen, and D. D. Joseph, "Lubricated pipelining: Stability of core-annular flow," J. Fluid Mech. **201**, 323–356 (1989).

[57]K. Chen, R. Bai, and D. D. Joseph, "Lubricated pipelining: Part 3 Stability of core-annular flow in vertical pipes," J. Fluid Mech. **214**, 251–286 (1990).

[58]M. Allouche, I. A. Frigaard, and G. Sona, "Static wall layers in the displacement of two visco-plastic fluids in a plane channel," J. Fluid Mech. **424**, 243–277 (2000).

[59]H. M. Caliman, E. J. Soares, and R. L. Thompson, "An experimental investigation on the Newtonian–Newtonian and viscoplastic–Newtonian displacement in a capillary tube," J. Non-Newtonian Fluid Mech. **247**, 207–220 (2017).

[60]D. A. de Sousa, E. J. Soares, R. S. de Queiroz, and R. L. Thompson, "Numerical investigation on gas-displacement of a shear-thinning liquid and a visco-plastic material in capillary tubes," J. Non-Newtonian Fluid Mech. **144**(2–3), 149–159 (2007).

[61]J. F. Freitas, E. J. Soares, and R. L. Thompson, "Viscoplastic-viscoplastic displacement in a plane channel with interfacial tension effects," Chem. Eng. Sci. **91**, 54–64 (2013).

[62]J. F. Freitas, E. J. Soares, and R. L. Thompson, "Immiscible Newtonian displacement by a viscoplastic material in a capillary plane channel," Rheol. Acta **50**(4), 403–422 (2011).

[63]C. Gabard and J. P. Hulin, "Miscible displacement of non-Newtonian fluids in a vertical tube," Eur. Phys. J. E **11**(3), 231–241 (2003).

[64]B. Lund, A. Taghipour, J. D. Ytrehus, and A. Saasen, "Experimental methods for investigation of drilling fluid displacement in irregular annuli," Energies **13**(19), 5201 (2020).

[65]L. Ren, J. Masliyah, and D. Li, "Experimental and theoretical study of the displacement process between two electrolyte solutions in a microchannel," J. Colloid Interface Sci. **257**, 85 (2003).

[66]R. L. Thompson, E. J. Soares, and R. D. A. Bacchi, "Further remarks on numerical investigation on gas displacement of a shear-thinning liquid and a visco-plastic material in capillary tubes," J. Non-Newtonian Fluid Mech. **165**(7–8), 448–452 (2010).

[67]E. J. Soares, M. S. Carvalho, and P. R. Souza Mendes, "Gas-displacement of non-Newtonian liquids in capillary tubes," Int. J. Heat Fluid Flow **27**(1), 95–104 (2006).

[68]T. Soori and T. Ward, "Stable and unstable miscible displacement of a shear-thinning fluid at low Reynolds number," Phys. Fluids **30**, 103101 (2018).

[69]R. L. Thompson and E. J. Soares, "Motion of a power-law long drop in a capillary tube filled by a Newtonian fluid," Chem. Eng. Sci. **72**, 126–141 (2012).

[70]E. Fabrízio Quintella, P. Roberto, S. Mendes, and P. Rio, in 10th Brazilian Congress of Thermal Sciences and Engineering (Brazilian Society of Mechanical Sciences and Engineering, 2004), pp. 0733_1–0733_10.

[71]E. Fabrízio Quintella, P. Roberto, S. Mendes, M. Da, and S. Carvalho, in *17th International Congress of Mechanical Engineering* ABCM, 2003.

[72]V. Gauri and K. W. Koelling, "Gas-assisted displacement of viscoelastic fluids: Flow dynamics at the bubble front," J. Non-Newtonian Fluid Mech. **83**, 183–203 (1999).

[73]P. E. Huzyak and K. W. Koelling, "The penetration of a long bubble through a viscoelastic fluid in a tube," J. Non-Newtonian Fluid Mech. **71**, 73 (1997).

[74]F. Kamisli, "Gas-assisted displacement of a viscoelastic fluid in capillary geometries," Chem. Eng. Sci. **61**(4), 1203–1216 (2006).

[75]S. Mora and M. Manna, "Saffman-Taylor instability of viscoelastic fluids: From viscous fingering to elastic fractures," Phys. Rev. **81**(2), 026305 (2010).

[76]S. Mora and M. Manna, "From viscous fingering to elastic instabilities," J. Non-Newtonian Fluid Mech. **173–174**, 30–39 (2012).

[77]B. Saintyves, S. Mora, and E. Bouchaud, "A meniscus fingering instability in viscoelastic fluids," Phys. Fluids **31**(6), 063108 (2019).

[78]E. J. Soares, P. R. De, S. Mendes, M. Da, and S. Carvalho, "Immiscible liquid-liquid displacement in capillary tubes: Viscoelastic effects," J. Braz. Soc. Mech. Sci. Eng. **30**(2), 160–165 (2008).

[79]P. Dontula, C. W. Macosko, and L. E. Scriven, "Model elastic liquids with water-soluble polymers," AIChE J. **44**(6), 1247–1255 (1998).

[80]F. A. Morrison, *Understanding Rheology* (Oxford University Press, 2001).

[81]K. Sadik, K. Shah Ramesh, and A. Win, *Handbook of Single-Phase Convective Heat Transfer*, 1st ed. (Wiley-Interscience, New York, 1987).

[82]S. Kenney, K. Poper, G. Chapagain, and G. F. Christopher, "Large Deborah number flows around confined microfluidic cylinders," Rheol. Acta **52**(5), 485–497 (2013).

[83]S. Migliozzi, L. Mazzei, and P. Angeli, "Viscoelastic flow instabilities in static mixers: Onset and effect on the mixing efficiency," Phys. Fluids **33**(1), 013104 (2021).

[84]X. Shi and G. F. Christopher, "Growth of viscoelastic instabilities around linear cylinder arrays," Phys. Fluids **28**(12), 124102 (2016).

[85]J. Y. Yoo and D. D. Joseph, "Hyperbolicity and change of type in the flow of viscoelastic fluids through channels," J. Non-Newtonian Fluid Mech. **19**, 15–41 (1985).

[86]S. S. Datta, A. M. Ardekani, P. E. Arratia, A. N. Beris, I. Bischofberger, G. H. Mckinley, J. G. Eggers, J. E. López-Aguilar, S. M. Fielding, A. Frishman, M. D. Graham, J. S. Guasto, S. J. Haward, A. Q. Shen, S. Hormozi, A. Morozov, R. J. Poole, V. Shankar, E. S. G. Shaqfeh, H. Stark, V. Steinberg, G. Subramanian, and H. A. Stone, "Perspectives on viscoelastic flow instabilities and elastic turbulence," Phys. Rev. Fluids **7**(8), 080701 (2022).

[87]A. Varshney and V. Steinberg, "Elastic Alfven waves in elastic turbulence," Nat. Commun. **10**(1), 652 (2019).

[88] A. Fouxon and V. Lebedev, "Spectra of turbulence in dilute polymer solutions," Phys. Fluids **15**(7), 2060–2072 (2003).

[89] T. Burghelea, V. Steinberg, and P. H. Diamond, "Internal viscoelastic waves in a circular couette flow of a dilute polymer solution," Europhys. Lett. **60**, 704 (2002).

[90] D. T. Papageorgiou, "Linear instability of the supersonic wake behind a flat plate aligned with a uniform stream," Theor. Comput. Fluid Dyn. **1**, 327 (1990).

[91] W. G. C. Boyd, "Shear-flow instability at the interface between two viscous fluids," J. Fluid Mech. **128**, 507–528 (1983).

[92] M. R. Driel and S. Ayyash, "Drag reduction in laminar flow," Nature **259**, 389–390 (1976).

[93] J. Azaiez A N and D. G. M. Homsy, "Linear stability of free shear flow of viscoelastic liquids," J. Fluid Mech. **268**, 37 (1994).

[94] P. Pakdel and G. H. Mckinley, "Elastic instability and curved streamlines," Phys. Rev. Lett. **77**, 2459 (1996).

[95] G. H. Mckinley, P. Pakdel, A. Oztekin, and G. H. Mckinley, "Rheological and geometric scaling of purely elastic instabilities," J. Non-Newtonian Fluid Mech **67**, 19–47 (1996).

[96] E. M. Ekanem, S. Berg, S. De, A. Fadili, and P. Luckham, "Towards predicting the onset of elastic turbulence in complex geometries," Transp. Porous Med. **143**(1), 151–168 (2022).

[97] Y. Y. Renardy, "Snakes and corkscrews in core-annular down-flow of two fluids," J. Fluid Mech. **340**, 297–317 (1997).